

Robotic Fencing Partner

Fall 2025 ME Executive Summary

Design Team

Josh Dillon, Peter Di Natale, Ethan Fisk, Shivansh Kumar, Zaki Loldj, Anson Mole

Design Advisor

Ms. Aparna Rector

Abstract

Despite major advances in sports robotics, fencing lacks a system capable of reproducing the high-speed, agile, and multi-directional wrist movements required for realistic bladework. Our team, with the guidance of Ms. Aparna Rector, conducted the research, design, and development of a robotic fencing partner aimed at enabling independent bladework training without reliance on a human opponent. This work draws on studies of sports robotics, human wrist biomechanics, and human-robot safety to establish the technical foundations of the system. Building on these findings, the team details the design specifications of a stationary base equipped with an arm and a three degree of freedom robotic wrist that replicates human motion. Also detailed is the development of wrist trajectories that were generated from motion-capture recordings of saber bladework, alongside dynamic simulations which informed transmission design, motor selection, and range-of-motion requirements. The multi-stage design process outlined in this work includes wrist mechanism comparison, iterative arm development, and structural analysis. Testing demonstrates that the design can achieve human-like speeds and ranges of motion, while replicating motion-capture paths with high accuracy. Together, these elements summarize the complete development of an accessible robotic platform for fencing-specific skill development, enabling independent and realistic training.



For more information, please contact a.alavilli@northeastern.edu

Need

The COVID-19 pandemic had a major impact on numerous sports around the US, with arguably one of the most impacted being fencing. Due to the one-on-one nature of the sport, as well as the need to practice indoors, fencing's governing body, USA Fencing, lost over 50% of its membership during the pandemic [1]. While these numbers are back on the rise, this situation emphasized how difficult it is to train for fencing without access to the proper facilities. This is not exclusive to the pandemic, however, as finding a place to practice is a common challenge faced by those who are new to fencing. Normally, fencing centers operate in large metropolitan areas, leaving residents of rural America with little to no options to get into the sport [1]. As a result, the fencing community is very small, comprising mostly of amateurs spread out around the country [2]. This project aims to fill this void, creating an option for fencers to either get started learning without a partner or supplement their current training schedule using an autonomous training partner. A successful robot that can teach a human and train with them would increase the scope of fencing in America and abroad, making it more accessible to a wider audience. Through this project, we have developed a robotic wrist, mounted on a stationary "fencing dummy", which can manipulate a fencing blade through a series of preprogrammed training routines. This will allow fencers to practice the repetitive but crucial blade work needed to be successful in the sport, without requiring a human training partner.

Background and Significant Prior Work

To design a robotic system capable of executing human-like fencing bladework, it was necessary to ground the project in research spanning sports robotics, human biomechanics, wrist mechanisms, and interactive robot safety. This section synthesizes the most relevant work from these fields, establishing the technical context that shapes the design requirements, performance targets, and safety constraints of the system.

Robotics has become an increasingly influential tool in sports training, particularly for one-on-one and high-speed sports where consistent, repeatable practice is essential. Robotic systems have been developed to remedy this issue for other one-on-one sports, such as table tennis. MIT and DeepMind have each developed table tennis robots, demonstrating high-speed actuation and trajectory control, allowing a table tennis player to practice effectively without a partner [3], [4]. These projects demonstrate how robotic platforms can compensate for the absence of a human opponent while maintaining realistic performance.

This project aims to apply this same type of solution to fencing. Currently, few attempts have been made to use robotic systems to aid fencers. Most of these attempts include hobbyist builds or limited prototypes [5], [6]. The most elaborate attempt was made by the German Fencing Federation. This system does provide an option for fencers to train independently, but it is limited by only achieving 1 degree of freedom motion, with slower than human-speed actuation [7]. This project serves to fill this gap with a robotic fencing wrist capable of replicating human-like bladework at realistic speeds.

Because fencing bladework relies on rapid and coordinated wrist articulation, understanding human biomechanics was central to defining our design targets. We identified the three degrees of freedom in a wrist: pronation/supination, flexion/extension, and radial/ulnar deviation [8]. We also compiled data for the human-level dynamics in each of these degrees of freedom, which helped guide our design benchmarks [9]. Motion capture methods helped further refine these requirements. We made use of Professor Max Shepherd's lab facility at Northeastern to capture marker-based tracking data [10]. This allowed us to determine accurate measurements of joint angles, velocities, and in-hand blade manipulation during realistic fencing actions, which helped establish the trajectory demands required by our robotic wrist.

To explore mechanisms capable of reproducing these human-like 3 DoF wrist motions, we reviewed existing robotic wrist systems such as the OpenWrist exoskeleton and the LIMS2-AMBIDEX manipulator [11], [12]. These designs achieved high dynamic performance and helped inform our mechanical design and control strategies to achieve responsive, backdrivable motion. The LIMS2-AMBIDEX manipulator mechanism uses remote actuation, placing all motors in the base, and transmits power via long cable systems [12]. The OpenWrist, however, used motors mounted closer to the wrist with shorter cable runs, resulting in higher stiffness but more inertia located near the end effector [11]. Understanding the differences in these highly effective wrist designs was crucial in helping us brainstorm candidate wrist designs for our wrist mechanism.

Another crucial part of our research process was understanding the safety principles for interactive robotics that would guide our safety requirements. These principles helped guide the integration of mechanical hard stops, software torque limits, and emergency shutoff systems to prevent injury or unsafe motion [13]. We also researched fencing safety requirements, including protective gear and typical injury risks, to ensure we test and utilize our robot in a safe manner [14].

Prior work across sports robotics, biomechanical analysis, robotic wrist mechanisms, and human–robot safety collectively informed the design of our system. These research findings defined the functional requirements for achieving realistic fencing motion, identified proven strategies for high-speed actuation and low-inertia wrist mechanisms, and established safety frameworks necessary for interactive athletic robotics. This foundation directly shaped the mechanical, electrical, and control design decisions presented in the remainder of this report.

Design Solution

Our design aims to mimic a human fencing partner that can perform training routines with a user at varying speeds to improve their muscle memory. The two primary components of our design are the base and the 3 DoF wrist. To fit our project within the timeline, we split up these components further to create 4 subsystems to design in parallel. The base consists of the 80/20 structure that will hold up the whole system and the posable arm design that will hold the wrist mechanism. Our team split the wrist mechanism into two subsystems, the differential assembly and the pronation-supination assembly. We will explore the varying design requirements and solutions for each of these subsystems in this section, in addition to how each of the components was manufactured.

Stationary Base

Early in the fall semester, our team met to clearly define the design requirements for the stationary base of our robot. We decided that the main priority for the base is that it will hold the shoulder steady and upright through all required wrist movements. This will ensure that the motors can output precise movements at high speeds. In addition to this most basic requirement, we want the base to provide mounting surfaces for any hardware or wiring originating at the wrist and would like to minimize weight for ease of use and transportation. We met these requirements with our choice of material, 80/20 aluminum extrusions, as they are lightweight and feature T-slots for customization.

We decided that the stationary base should mimic the proportions of an average human. This decision lets us fit the robot with an electrified fencing uniform so that the user can “hit” the robot for additional training feedback, as well as provide a realistic sight picture for someone who is training to fight a real opponent. The arm/base team referenced anthropometric data to find the average values for humans and determine the lengths of our links. The important values for the stationary base are the shoulder height and shoulder width, which were found to be 56” and 17”, respectively [15]. We designed the base so that it includes a

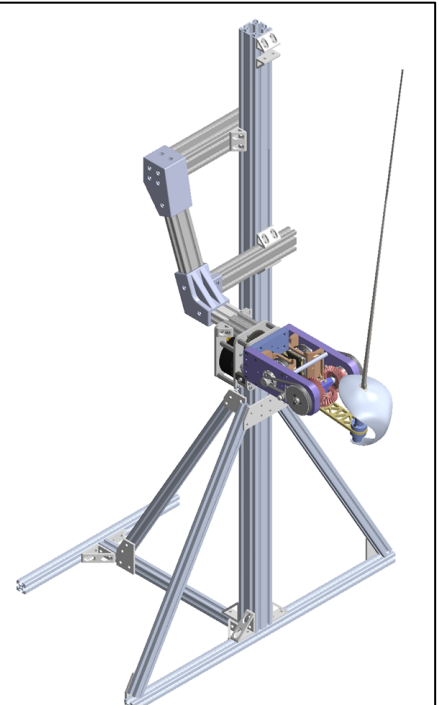


Figure 1: Design for the base of the robot made of 80/20 extrusions

central 2" x 2" 80/20 post that is 60" long to allow for height adjustability but remains around the average height for a human shoulder. The width of the top crossbar as seen in Figure 1 is 17", which makes the top of the base resemble the general dimensions of the average human [15].

Our current design achieves the lightweight goal by using aluminum 80/20 links that are lightweight and provide the structure with the proper stiffness. The total weight of our base is under 15 pounds, allowing for easy transportation of the entire system. However, we needed to incorporate counterweights into the system to ensure stability once the wrist mechanism is mounted and actuated. For this, we have acquired around 100 pounds in free weights and sandbags to maintain stability.

Passive Arm

The passive arm design seen in Figure 1 implements a structurally reinforced fixed-beam configuration that ensures end-point rigidity at the wrist mounting point. By establishing a fixed structural connection between the elbow joint and a mounting point on the vertical base post, the cantilevered arm configuration is transformed into a dual-supported beam that effectively resists bending about the base's primary axes. The upper arm is oriented at a 20-degree angle to minimize the moment arm distance between the wrist mounting point and the vertical base post connection, thereby reducing angular deflection at both interfaces. This geometric configuration aligns the primary structural member with the gravitational load vector, maximizing the arm's resistance to vertical deflections while maintaining a compact footprint within the robot's workspace.

All structural joints and mounting brackets are 3D printed with 50% infill density and increased wall thickness to maximize rigidity and minimize compliance throughout the load path. The 1"x2" 80/20 aluminum extrusion profile was selected to act as the arm segment because of its high second moment of area and axial rigidity, providing superior resistance to bending and torsional deflection compared to smaller profile alternatives.

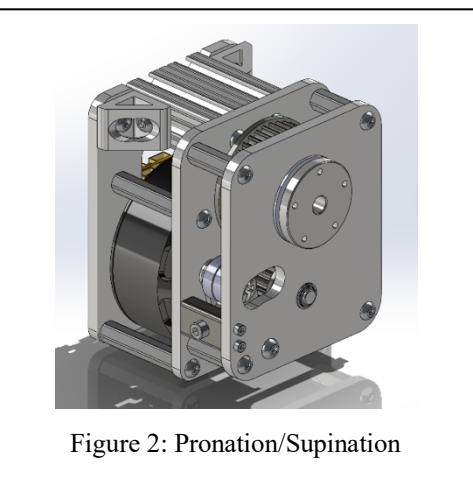


Figure 2: Pronation/Supination

Pronation Supination Joint

The pronation-supination joint (see Figure 2) is the larger joint located at the base of the wrist and is named after the human wrist motion which it approximates. This joint is responsible for the "roll" motion of the wrist, and it has the largest torque and speed requirements based on our dynamic analysis. Due to the large moment of inertia of both the blade (in the upright position) and the added mass of additional wrist components downstream of this joint, a large motor is required to achieve our desired trajectories.

Based on motor selection analysis, the ODrive M8325s used in this design needed a ~2:1 ratio or higher to comfortably achieve our torque requirements, so this joint implements a 2:1 belt reduction with 20T and 40T 5mm HTD pulleys. These pulleys are 3D printed and bolted onto custom machined shafts which provide the transmission with the necessary

torsional strength. Each of these shafts is double supported with flanged bearings on either side, pressed into the 3d printed frame pieces.

The joint also provides a hollow output shaft to pass wires through to the two motors located downstream of this joint, which simplifies wire routing, minimizes the exposure of the wires to the user, and minimizes the risk of snagging. The frame of the joint consists of three flat 3d printed plates which are bolted together using threaded standoffs. This creates a rigid assembly from which the PS joint can be mounted to the arm of the static frame. These plates are designed to be easily replaced with carbon fiber alternatives for increased rigidity, as none of the plates have any threaded holes, which may be problematic to create in thin carbon fiber plates. The arm is made using 80/20 aluminum extrusions, which slot into the corresponding gap in the back panel and bolt onto the center frame plate. The larger flanged section of the output shaft provides the attachment point for the rest of the differential wrist mechanism, which bolts on to the face of the flange to create a rigid connection. Detailed analysis of this output shaft is presented in Appendix A.

Differential Wrist Mechanism

The primary purpose of the differential wrist mechanism is to replicate two of the three main types of human wrist motion: radial/ulnar deviation (responsible for the “pitch” motion) and flexion/extension (responsible for the “yaw” motion).

To achieve these motions, a set of three bevel gears is driven by two MJbots MJ5208 BLDC motors through a 4:1 gear reduction. This ratio is implemented using an 18-tooth pulley attached to each motor, which drives a 72-tooth pulley connected to the bevel gears on the side of the differential (as shown in Figure 3). The pulleys are linked with a Powergrip GT3 3 mm-pitch belt that is 9mm wide, selected for its ability to deliver high torque without ratcheting with low positioning error [16]. With an adjustable mechanism, these belts were preloaded to ~50 Newtons of tension to ensure one side would not go slack under peak torque and prevent belt ratcheting.

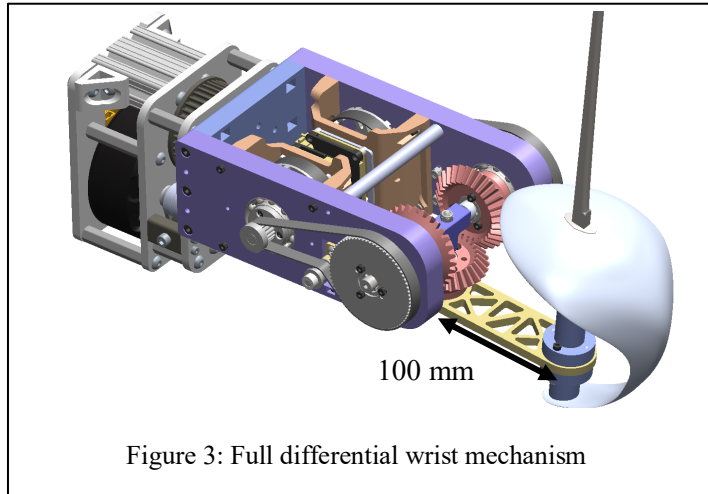


Figure 3: Full differential wrist mechanism

The differential used in this subsystem contains 3 bevel gears supported by steel shoulder bolts and constrained by 4 ball bearings (2 per side). To minimize weight, the bevel gears are FDM 3D-printed with CF-PLA and fixed to a custom-machined aluminum hub. Each pulley is also 3D printed and fastened to the aluminum hub and bevel gear using screws and dowel pins for alignment.

At the front of the assembly, the fencing blade is mounted to a waterjet-cut aluminum plate connected to the bottom of the bevel gear. To replicate the range of motion of a human wrist, this plate offsets the blade from the center of rotation by roughly 100 mm, which corresponds to an average human wrist geometry. Because this offset introduces a significant moment about the center of the differential, the plate was made from aluminum to ensure stiffness and strength.

Because a user will be interacting with this mechanism, additional safety considerations were discussed to eliminate potential risks in an interview with Northeastern’s building safety manager, Christopher Stoney [17]. To ensure the robot can safely be used, calculations were done to determine the maximum pressure that a user feels when hit by the blade. These results proved that the pressure the user feels falls significantly

below the 100-psi threshold that is reported to cause pain. Beyond further developing our SOP, a 3D printed guard was created to protect the blade from being pinched into the pulley/belt interface [18].

Summary

The robotic fencing partner is designed with 4 main subsystems to mimic human movement: a stationary base and a passive arm, each made of 80/20 extrusion and dimensioned to resemble a human torso, a 3 DoF wrist mechanism for blade manipulation. The wrist is divided into a pronation-supination joint for roll and a bevel gear differential joint for pitch and yaw. The system uses high torque motors and low gear reductions to achieve highly dynamic movements.

Design Process

The design process was advanced along two parallel tracks: the development of the base and arm structure and the design of the 3-DoF wrist that was supported by it. This began with the conduction of a motion-capture study of a fencer. The data were then processed to isolate wrist movement and to extract the blade trajectories that needed to be replicated by the robot. As design concepts were generated, each one was tested in a virtual environment for its ability to achieve these trajectories. Dynamic analyses were then performed in Simulink to determine the motor torques required for each candidate design. By comparing these results with the design objectives, the optimal configuration for the robot was selected.

Development of Arm Joints

Several arm-joint designs were considered to meet the base's primary design requirement of providing a stiff, stable support structure for the actuated wrist. Because the system did not require a fully articulated arm, minimizing vibration, deflection, and unwanted motion was prioritized so the wrist could accurately follow commanded trajectories. Posable adjustability was also considered to accommodate different operating angles.

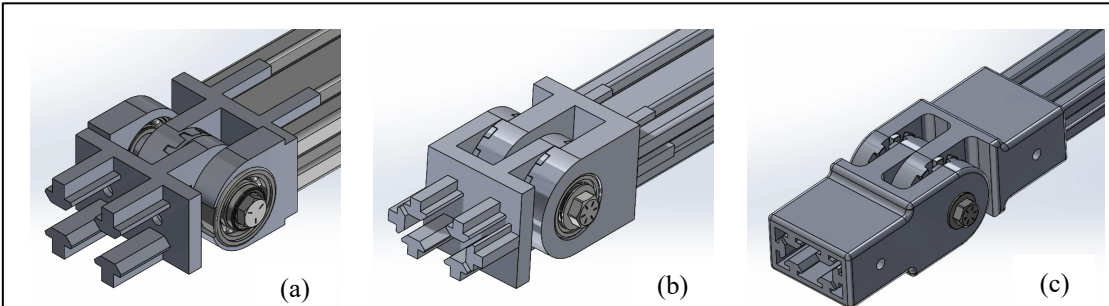


Figure 4: Development of the posable arm hinges over time
 (a) 1st Iteration (b) 2nd Iteration (c) 3rd Iteration

The first design was a static elbow joint to enable rapid integration and initial wrist testing. After validating the wrist, adjustable designs were considered. The first adjustable iteration used a single-ear clevis with a Hirth joint (Fig. 4a). Strength testing showed that this configuration lacked sufficient load capacity. This was addressed in the second iteration by adding a second clevis ear and increasing print strength through infill and pattern changes (Fig. 4b). Testing then revealed a new weakness at the clevis–baseplate interface. In the third iteration, a sleeve was introduced to better secure around the 80/20 extrusion, and an increased wall thickness was used to improve structural robustness (Fig. 4c).

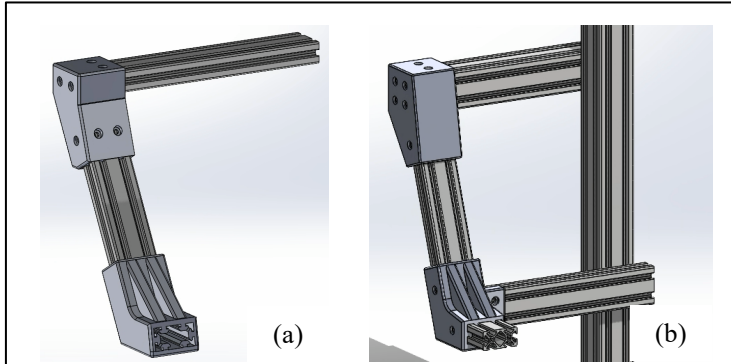


Figure 5: Development of the Fixed Arm
 (a) 1st Iteration (b) 2nd Iteration

After integrating the final adjustable joint, dynamic testing showed that high-torque wrist motions produced measurable position error due to flexure in the multi-segment arm, which behaved as a cantilever. To eliminate this compliance, a secondary support was added between the elbow and the vertical base beam. This reinforcement required fixing the elbow at a single angle to ensure alignment with the base, leading us to readopt a static elbow design (figure 5b) that maximized stiffness and wrist stability.

Motion Capture Analysis

To quantify the motion requirements for the robotic wrist, a comprehensive motion capture study was conducted from early August through the end of September. The analysis included four main phases: data collection, post-processing, wrist motion isolation, and conversion of the measured motion into executable robot trajectories. The resulting datasets were subsequently used to evaluate candidate wrist designs, select actuators, and define the range of motion.

Data Collection

Data were collected in the Northeastern University motion capture lab (Richards Hall, 4th floor) with access and technical support from the Shepherd Lab [10]. Marker placement protocols were established in consultation with Jessica Geiger from New Balance Sports Research, following her recommendations for reliable wrist and hand tracking [19]. Figure 6 shows some of the markers as they were attached to the arm, as well as the blade which was covered in masking tape to eliminate infrared reflections. Using this setup, several trials were recorded, including those which captured wrist-dominant saber fencing movements with minimal arm contribution, ensuring that the captured data primarily represented hand and wrist articulation. Data were collected using ~19 cameras sampling 3D position of 11 markers at 300Hz.

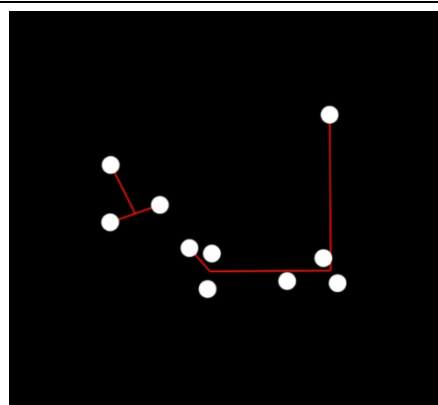


Figure 7: Post-processed kinematic chain with blade (left) and arm (right)



Figure 6: Motion capture marker placement

Post-Processing

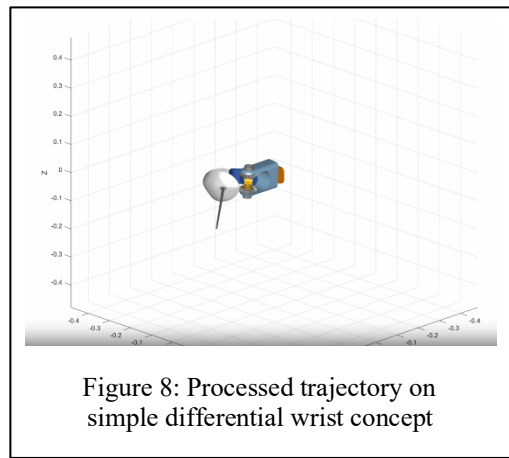
Collected marker data were processed using the MATLAB-based *MoCap Toolbox* [20] with additional custom scripts. Because occlusion occasionally caused marker IDs to lose tracking and be reassigned, an automated script was developed to identify and merge duplicate IDs based on temporal overlap and spatial proximity between disappearing and reappearing markers. Once duplicates were removed, a table defining marker labels was manually created for each trial. Markers representing “hand” or “shoulder” for example were not consistently given the same ID across trials and

therefore needed to be manually associated with meaningful labels. Connectivity was then defined along a simplified kinematic chain from shoulder to hand (see Figure 7), with an additional set of markers defining the blade and guard geometry. Small positional offsets (≈ 20 mm) were applied to correct for marker mounting height, which improved the accuracy of reconstructed motion. This is necessary as the blade for example is relatively thin, so the offset created by mounting a marker on the side results in significant angular error when compared to the blade center line. Modified toolbox functions were then used to visualize and validate each processed trial.

Wrist Motion Isolation

To derive realistic wrist-only motion, all translational movement relative to the wrist center of rotation was removed, leaving only the relative rotation of the hand and blade. A “wrist link” vector was defined as the minimum-distance line perpendicular to the blade vector, representing a rigid robot link orthogonal to the blade. The time-varying orientation of this link was calculated as a series of rotation matrices, forming the reference trajectory for wrist design.

An additional modeling scheme explored introducing a fourth degree of freedom (DoF) to emulate the subtle in-hand manipulation characteristic of fencing. This DoF, defined by the angular relationship between the wrist–hand and hand–blade vectors, was tested in simulation. Although it slightly reduced wrist range of motion, the added complexity was deemed unnecessary for the current prototype, as the baseline three-DoF configuration resulted in range of motion requirements that were achievable.



Robot Trajectory Generation

Processed MoCap trajectories were imported into MATLAB’s *Robotics System Toolbox* using URDF models exported from Onshape via the *Onshape-to-Robot* [21] plugin. Inverse kinematics were solved for multiple candidate wrist mechanisms to reproduce the measured blade orientation while constraining position weights to zero. Animated visualizations were rendered to compare designs including serial/differential, and parallel wrists (see Figure 8).

This analysis revealed that certain configurations (e.g., serial XYX) suffered from singularities, while others (e.g., serial Z joint + differential wrist) exhibited low inertia but produced motion that was not human-like. The most balanced solutions

were selected for subsequent dynamic modeling and hardware prototyping.

Dynamic Analysis

Filtering Motion Capture Joint Angle vs. Time Data

Due to the high sampling frequency of the motion capture data and the need to take derivatives of the data to perform a dynamic analysis, significant noise amplification occurred during initial Simscape dynamic modeling. To alleviate the joint angular position, velocity, and acceleration timeseries data were pre-computed and filtered in a custom MATLAB script before being inputted into simulation; this was a necessary step to have control over the filtering process and is shown in Figure 9. Additionally, this process was manually validated to prevent filtering overcorrection by manually computing derivatives using hand-calculations on a sinusoidal portion of the joint angle vs. time data. A Savitsky-Golay filter was chosen due

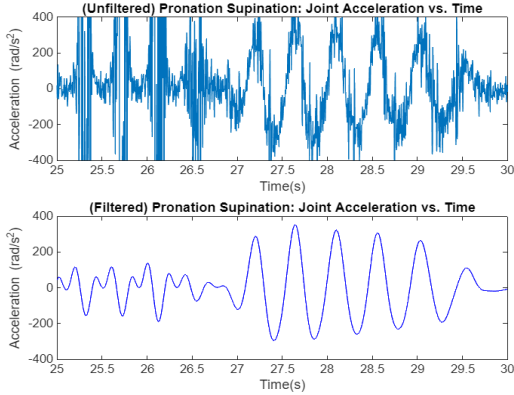


Figure 9: Noise Reduction After Filtering of Joint Angle Data

modeled and proper materials were assigned. Initially, the fencing blade was simplified to a steel rod of similar dimensions; however, this approximation produced inflated torque results that would be out of reach for a human [23] due to the fact that the center of mass of an actual fencing blade is biased closer to the wrist. As a result, an accurate model of the fencing blade was created in CAD, which improved the fidelity of the simulation. After obtaining the required torques at each joint, the results were translated to torques required for each motor as the differential mechanism has two motors working together to actuate two degrees of freedom. These results were then used to decide on motors for the design.

Further experimentation was also done in simulation to see the sensitivity of the mechanism to factors that may cause changes in inertia. It was discovered that the fencing blade is the dominant inertia in the mechanism, and changes such as motor mounting locations did not significantly change inertia. This discovery allowed for additional design freedom in structural material choice, motor choice, and transmission mounting location.



Figure 10: Visualization of Input Trajectories to Mechanism in Simscape

Wrist Mechanism Selection

The wrist mechanism for this project must achieve human-like range of motion, speed, and controllability within compact, manufacturable constraints. To identify the most effective wrist mechanism to achieve these goals, we set up a multi-stage design evaluation with candidate designs. The team began with a brainstorming phase, sketching and CAD modeling multiple potential 3 DoF wrist designs. We identified seven designs that fulfilled our requirements and put them into a decision matrix. In this matrix, we defined twelve selection criteria that were used to evaluate the overall design: *Sensitivity to Tolerances, Peak Torque Requirement, Range of Motion, Compactness/Weight, Controllability, Durability/ Maintenance, Wiring Complexity, Cooling Complexity, Manufacturability, Transmission Complexity, Uniqueness, Cost*. Each team member independently assigned percentage weights to these criteria, reflecting their relative importance, and we averaged these values to determine the weights for these criteria. For each candidate

to its ability to preserve the shape of an input signal and not phase shift data [22]. After experimentation, a filter which fits a 5th order polynomial to a frame size of 99 points was chosen as it proved to strike a balance between smoothing noise and not decreasing the amplitude of the response.

Simulink/Simscape Model

A dynamic analysis of the wrist mechanism was performed in Simscape/Simulink to determine the actuator torques required to achieve the motion capture trajectories (see Figure 10). To obtain accurate results but not significantly increase computation time, the main structural, transmission, and carried motors of the design were

mechanism, the team assigned 1-5 performance scores per criterion, based on analysis that was done on each mechanism. To minimize comparative bias, total scores for other candidates were hidden as we moved through them. The decision matrix results clearly identified one mechanism as the top performer based on overall weighted score, achieving the best balance of range of motion, speed & torque efficiency, and controllability, while maintaining manageable manufacturing complexity and motor design. This process allowed us to move forward with the differential wrist design with confidence, knowing that all team members supported the idea that this design was the most feasible pathway to achieving human-like motion performance.

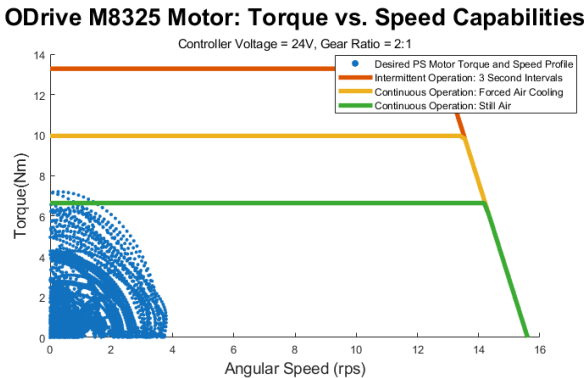


Figure 11: ODrive Motor Operating Regime and Desired PS Motor and Torque Profile

Motor Selection Process

Since fencing is a highly dynamic task, motor selection and transmission design were a key highlight of our robot. The dynamic simulation showcased the high torque requirements for motors, reaching upwards of 3 Nm for the differential motor and 7.5 Nm for the pronation/supination motor. Additionally, achieving the quickly changing torque trajectories shown by the motion capture requires a low gear ratio transmission [24]. As such, the search for motors was restricted to BLDC motors due to their high torque density.

The equations representing the operating regimes for a BLDC motor were copied from the simulation tool provided by ODrive Motors [25]. With listed specifications for a motor such as its coil resistance, coil inductance, number of poles, continuous current capabilities without cooling, continuous current capabilities with cooling, peak current capabilities, and controller voltage, every combination of torque and speed that the motor can achieve was determined. With this, the application specific motor torques, and speeds were plotted against the motor's operating regimes with various transmission ratios to determine which motor and transmission ratio could work for the differential and PS joints. Figure 11 represents the requirements for the PS motor, with a very similar graph being generated for the differential motors.

As shown by the graph, the ODrive M8325S can achieve all the requirements posed by the dynamic analysis with a 2:1 gear ratio. In a similar manner, the MJ5208 motor can achieve differential joint requirements with a 4:1 gear ratio. These ultra-low gear ratios offer major advantages to the robot, allowing it to achieve large torque bandwidths that are well-suited for the agile maneuvers required in sports. Additionally, the low gear ratios make the robot significantly more backdrivable, increasing both the safety and realism of the training partner.

Summary

Our design process advanced along two parallel tracks: developing the base/arm structure and the 3-DoF wrist it supports. Motion-capture data from a fencer informed our project requirements and defined the wrist trajectories the system must reproduce. We evaluated multiple design concepts in a virtual environment, then performed dynamic analyses in Simulink to determine motor torque demands. Comparing these results allowed the team to select the most effective overall design.

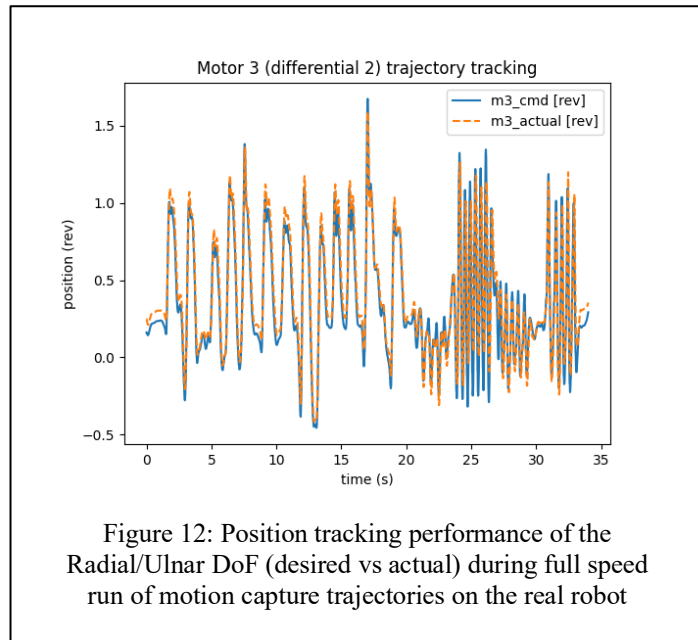
Results

Our most important performance metric is based on the robotic wrist's ability to accurately manipulate a fencing blade when compared to the motion capture data we have collected of a fencer in action. Crucially, since the motion capture data were recorded for a human participant at moderate to high exertion, if the robot can reproduce this motion, it would represent conclusive evidence of the system's 'human-like' dynamic ability.

Table 1: Desired vs. Actual Speeds and Range of Motion

DOF	ROM Desired	ROM Actual	Max Speed Desired	Max Recorded Speed*
P/S	0.55 rev.	0.55 rev. +	3.6 rev./s	3.6 rev./s
R/U	0.35 rev.	0.35 rev. +	2.2 rev./s	2.6 rev./s
F/E	0.23 rev.	0.23 rev. +	1.6 rev./s	1.9 rev./s

commands to each of our 3 motor drivers simultaneously, in the form of both position commands and desired velocity upon reaching those positions. Data were sent at 300Hz to the robot, and telemetry was recorded back at 100Hz from each of the drivers, consisting of actual position, velocity, and torque at each moment in time. Table 1 illustrates the extent which our motion capture goals were achieved, measured from peak values seen while running full speed motion capture trajectories on the real robot.



As part of our analysis, our motion capture trajectory was post-processed to the point of being clean and ready to run on our 3-dof wrist. A series of Python programs were created to run pre-programmed trajectories by sending

More specifically, Figure 12 shows the performance of the output of the radial ulnar joint during full speed testing. The orange line indicates our actual joint positions compared to our commanded positions in blue. These motions are reconstructed from the reported telemetry from both differential motors to show their combined output in the blade cutting (R/U) direction. We show here that the robot achieves high fidelity trajectory tracking, beyond simply achieving speed and range of motion goals, the system can reproduce fully dynamic, human-like motion, including subtle position changes at high speed.

Additionally, the robot can exert the high torques expected of it. As an example, these measured values for the pronation/supination joint closely match our expected torques. The measured torque values are estimated by the brushless motor controller from the motor current draw after an automatic calibration

process to determine the torque constant. These values should map with high accuracy to the output torque of the robot given the low gear ratios used in the design. As indicated in the motor selection section, the P/S motor is expected to require 7.5 Nm based on dynamic analysis, a value which mostly matches the values seen in Figure 13, with the actual measured value being ~1.4 Nm higher than expected.

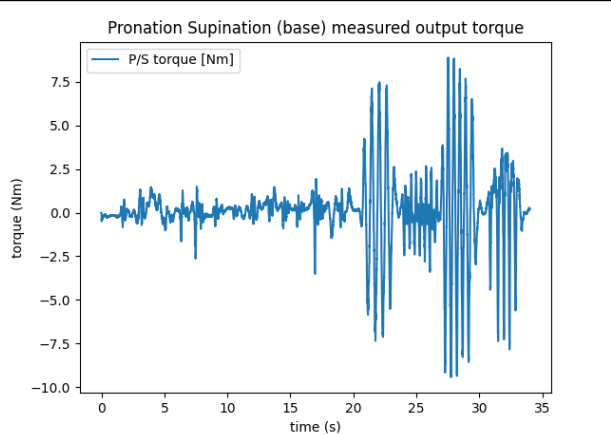


Figure 13: Pronation/Supination measured joint torque during full speed run of motion capture

Preliminary versions of a number of other tests were also conducted and filmed for review later, including teleoperation, where a custom controller is used to mimic the actions of a human operator, fencing drills with a partner and a human operator in control, and preprogrammed motions based on recorded waypoints rather than motion capture.

Teleoperation was shown to be very responsive and useful when conducting drills with a human in the loop controlling the robot during fencing drills. Certain fencing actions such as parries, including circle parries, cuts, and beats were all experimented with during live testing with an opponent, and the system was able to reproduce many of these actions with high fidelity, despite its lack of arm mobility. Although these results are not quantitative, they illustrate some success towards the goal of developing an interactive fencing partner.

Summary and Impact

Our project set out to address a gap in fencing, a sport with limited access to modern robotics. By creating a robotic training partner, we explored new technical skills while turning an idea into a functional system. Since many people lack access to fencing clubs or space to practice at home, this project could broaden participation and support long-term growth in the sport. This work also offers a foundation for future engineers or researchers interested in bringing more robotics to athletics. This project could be expanded to include an actuated arm, though this would increase the need for safety precautions.

Overall, this experience strengthened our engineering abilities and teamwork. Our solution provides an example others can build upon, showing how robotics can support niche communities like fencing and other sports with smaller participation. Completing this capstone project made us more capable problem-solvers as we continue forward with our professional careers.

References

- [1] I. Chirashnya, “12 Disadvantages of Fencing,” Academy of Fencing Masters. Accessed: July 14, 2020. [Online]. Available: <https://academyoffencingmasters.com/blog/12-disadvantages-of-fencing/>
- [2] I. Chirashnya, “How Accessible is Fencing,” Academy of Fencing Masters. Accessed: July 14, 2025. [Online]. Available: <https://academyoffencingmasters.com/blog/how-accessible-is-fencing/>
- [3] D. Nguyen, K. D. Cancio, and S. Kim, “High Speed Robotic Table Tennis Swinging Using Lightweight Hardware with Model Predictive Control,” May 02, 2025, *arXiv: arXiv:2505.01617*. doi: 10.48550/arXiv.2505.01617.
- [4] D. B. D’Ambrosio *et al.*, “Achieving Human Level Competitive Robot Table Tennis,” May 01, 2025, *arXiv: arXiv:2408.03906*. doi: 10.48550/arXiv.2408.03906.
- [5] L. Solondz, *Automated Lifelike Fencing Robotic Drilling Dummy (ALFRDD)*, (May 14, 2017). Accessed: July 18, 2025. [Online Video]. Available: <https://www.youtube.com/watch?v=Rac1QtWng0c>
- [6] I. Erausquin, *Fencing Robot Demo*, (Sept. 09, 2013). Accessed: July 18, 2025. [Online Video]. Available: <https://www.youtube.com/watch?v=kKKQQUMBqts>
- [7] M. Weichenberger, V. Schilling-Kästle, L. Mentz, T. Engleder, and M. Hessling, “A fencing robot for performance testing in elite fencers,” *Sports Technology*, vol. 8, no. 3–4, pp. 95–99, Oct. 2015, doi: 10.1080/19346182.2015.1108326.
- [8] H. Fan, G. Wei, and L. Ren, “Prosthetic and robotic wrists comparing with the intelligently evolved human wrist: A review,” *Robotica*, vol. 40, no. 11, pp. 4169–4191, Nov. 2022, doi: 10.1017/S0263574722000856.
- [9] Y. Jia, “Biomechanical analysis of fencing techniques: Insights from motion capture and analysis,” *Molecular & Cellular Biomechanics*, vol. 22, no. 3, Art. no. 3, Feb. 2025, doi: 10.62617/mcb1134.
- [10] M. Shepherd, “Biomechanics & Motion Capture Discussion,” July 29, 2025.
- [11] E. Pezent, C. G. Rose, A. D. Deshpande, and M. K. O’Malley, “Design and characterization of the OpenWrist: A robotic wrist exoskeleton for coordinated hand-wrist rehabilitation,” in *2017 International Conference on Rehabilitation Robotics (ICORR)*, July 2017, pp. 720–725. doi: 10.1109/ICORR.2017.8009333.
- [12] Y.-J. Kim, J.-I. Kim, and W. Jang, “Quaternion Joint: Dexterous 3-DOF Joint Representing Quaternion Motion for High-Speed Safe Interaction,” in *2018 IEEE/RSJ International Conference on Intelligent Robots and Systems (IROS)*, Madrid: IEEE, Oct. 2018, pp. 935–942. doi: 10.1109/iros.2018.8594301.
- [13] A. Nasr, K. Inkol, and J. McPhee, “Safety in Wearable Robotic Exoskeletons: Design, Control, and Testing Guidelines,” *Journal of Mechanisms and Robotics*, vol. 17, no. 050801, Nov. 2024, doi: 10.1115/1.4066900.
- [14] “Learn About Saber Fencing | Bergen Fencing Club, New Jersey,” Bergen Fencing Club. Accessed: Aug. 14, 2025. [Online]. Available: <https://bergenfencingclub.com/sabre-fencing/>
- [15] C. Gordon, “Anthropometric Data.” Anthropology Research Project Inc, Mar. 1989. Accessed: Oct. 01, 2025. [Online]. Available: <https://multisite.eos.ncsu.edu/www-ergocenter-ncsu-edu/wp-content/uploads/sites/18/2016/06/Anthropometric-Detailed-Data-Tables.pdf>
- [16] SDPSI, “Timing Belts, Pulleys, Chains, and Sprockets,” Handbook of Timing Belts, Pulleys, Chains and Sprockets. Accessed: Nov. 25, 2025. [Online]. Available: <https://sdp-si.com/D820/PDFS/Technical-Section.pdf>
- [17] C. Stoney, “Fencing Robot Safety Meeting,” Nov. 07, 2025.
- [18] “High pressure injection injury,” *Wikipedia*. July 22, 2025. Accessed: Nov. 26, 2025. [Online]. Available: https://en.wikipedia.org/w/index.php?title=High_pressure_injection_injury&oldid=1302011562
- [19] J. Geiger, “NewBalance Sports Research Discussion,” Aug. 06, 2025.
- [20] B. Burger and P. Toiviainen, “MoCap Toolbox - A Matlab toolbox for computational analysis of movement data.,” in *Proceedings of the Sound and Music Computing Conference 2013*, Stockholm, Sweden: Logos Verlag Berlin, 2013, pp. 172–178.
- [21] Rhoban/onshape-to-robot. (Nov. 10, 2025). Python. Rhoban. Accessed: Nov. 10, 2025. [Online]. Available: <https://github.com/Rhoban/onshape-to-robot>
- [22] “Savitsky Golay Filter,” *Wikipedia*. 2025. [Online]. Available: https://en.wikipedia.org/wiki/Savitzky%20%2893%29Golay_filter
- [23] K. Plewa, J. R. Potvin, and J. P. Dickey, “Wrist rotations about one or two axes affect maximum wrist strength,” *Applied Ergonomics*, vol. 53, pp. 152–160, Mar. 2016, doi: 10.1016/j.apergo.2015.09.005.
- [24] B. Katz, “A low cost modular actuator for dynamic robots,” MIT, Graduate Thesis, 2018. Accessed: Nov. 25, 2025. [Online]. Available: <https://dspace.mit.edu/handle/1721.1/118671>
- [25] “ODrive Motor Characteristics,” ODrive Robotics. Accessed: Nov. 01, 2025. [Online]. Available: <https://docs.odriverobotics.com/v/latest/hardware/odrive-motors.html#id8>
- [26] J. Pieper, “MJBots 5208,” MJ5208 Brushless Motor. Accessed: Nov. 25, 2025. [Online]. Available: <https://mjbots.com/products/mj5208>
- [27] R. G. Budynas, K. J. Nisbett, J. K. Nisbett, and J. E. Shigley, *Shigley’s mechanical engineering design*, 10. ed. in SI units. in McGraw-Hill series in mechanical engineering. New York, NY: McGraw-Hill Education, 2015.
- [28] McMaster-Carr, “Flanged Ball Bearing 15mm,” Flanged Ball Bearing. Accessed: Nov. 25, 2025. [Online]. Available: <https://www.mcmaster.com/4390N165/>
- [29] McMaster-Carr, “Flanged Ball Bearing 30mm.” Accessed: Nov. 25, 2025. [Online]. Available: <https://www.mcmaster.com/4390N181/>

Appendix A: Pronation/Supination Joint Shaft Failure Analysis

Introduction

The above fencing robot achieves blade manipulation using a 3 DoF serial wrist mechanism. Two motors work together in a differential joint to control the Radial/Ulnar (RU) and Flexion/Extension (FE) degrees of freedom, while one motor works to move the Pronation/Supination (PS) joint. The shaft of the PS joint requires additional consideration as it crucially supports the weight of the differential mechanism/blade, experiences the high external loads caused by the blade interacting with another fencer's blade, and must have enough internal clearance to route power and data cables to downstream motors. As a result, we conducted static loading design calculations together with a finite element analysis on this piece to ensure its proper function.

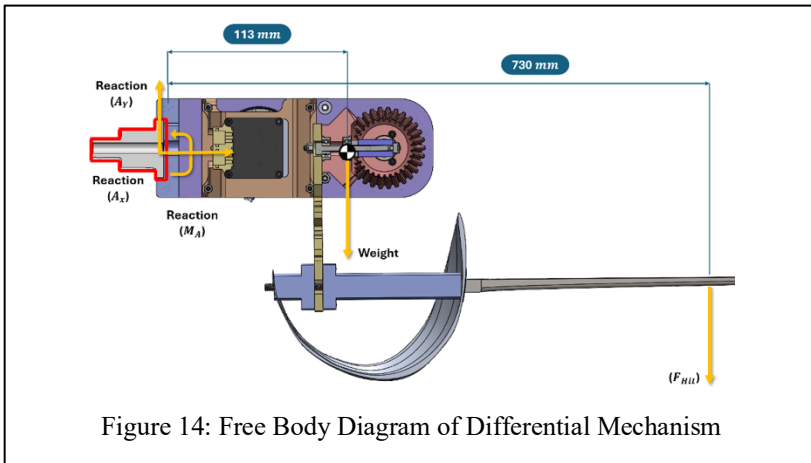


Figure 14: Free Body Diagram of Differential Mechanism

Methodology

To conduct static analysis on the shaft, SolidWorks FEA was used, with hand calculations being performed to both derive reaction loads and verify the FEA configuration was accurate. A MATLAB script was also written to efficiently test different loading scenarios and generate shear/bending moment plots.

The two main loads experienced by this shaft (outlined in red in

Figure 14) are the weight of the differential assembly/blade and the external force caused by a blade impacting another blade. Firstly, the weight and COM location of the differential assembly and blade were determined from the SolidWorks assembly. The maximum magnitude and location of F_{Hit} were then determined by identifying the two main limiting factors, the maximum output torque of the differential motors and the maximum torque that can be transmitted through the belts before ratcheting occurs. Since the GT3 3mm pitch timing belts were carefully chosen and preloaded to ensure they wouldn't ratchet under peak torque, the limiting factor was determined to be the motors. With the factory recommended torque limit of the MJ5208 motors being 1.7 Nm [26], the belt transmission ratio being 4:1 for both motors, and the two motors working together to achieve a cutting motion, the maximum moment that F_{Hit} can produce about the motors before they are back driven is 13.6 Nm. F_{Hit} 's location was chosen to be 500 mm from the base of the blade to replicate a realistic blade impact scenario and model a larger magnitude force as a worst-case scenario. To achieve the 13.6 Nm moment about the motor from this distance, the magnitude of F_{Hit} was determined to be 27.2 N. Additionally, the force applied to the blade (F_{Hit}) was assumed to be perpendicular to the blade and acting in the same direction as the weight of the wrist, which maximizes the reaction force (A_y) and reaction moment (M_A) experienced at the base of the cantilever. The following image shows how the differential wrist and the blade can be modeled as a cantilever with support reactions, which will be transmitted onto the PS joint shaft.

Opposite and equal reaction loads are thus applied to the PS shaft. A diagram of this joint is shown in Figure 15 with bearing supports at B1 and B2. Once the bearing loads were verified, a beam analysis was conducted to determine the shear force and bending moment along the length of the shaft. The plot was generated based on calculations performed in the MATLAB script. The values for shear force and bending moment were taken from this figure to calculate the associated stresses experienced by the beam. Because the shaft is not a constant diameter, the maximum bending stress and transverse shear stress had to be

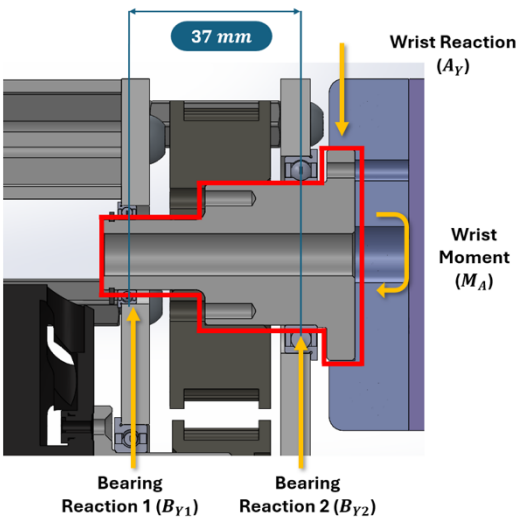


Figure 15: Free Body Diagram of PS Joint Shaft

calculated for each of the three different diameters (D_1 , D_2 , and D_3). The bending stress was calculated using the equation below:

$$\sigma_{bending} = \frac{M_{Max}r_o}{\frac{\pi}{64}(r_o^4 - r_i^4)} \quad (1)$$

Where $\sigma_{bending}$ is the max bending stress in each cross section, M is the maximum bending moment in each section of the beam, r_o is the outer radius of the section, r_i is the inner radius of the section.

The shear force diagram was also used to calculate the maximum transverse shear stress experienced by each part of the shaft. The following equation was used to calculate the shear stress for a beam with a hollow circular cross section.

$$\tau_{transverse} = \frac{3V_{max}}{4A} \frac{(1+Dd)}{(d^2 + D^2)} \quad (2)$$

Where $\tau_{transverse}$ is the maximum transverse shear stress in each cross section, V is the maximum shear force in each section of the beam, D is the outer diameter of the section, d is the inner diameter of the section.

The maximum transverse shear stress and the maximum bending stress were each located on the smallest shaft diameter, D_1 . Additionally, this smallest diameter shaft has a fillet radius at the location of highest bending stress, whose stress concentration was calculated by referencing Shigley's design charts, as seen in figure 17 [27].

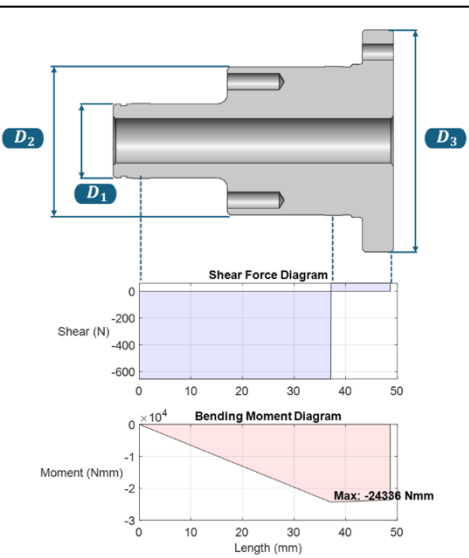


Figure 16: Shear Force and Bending Moment diagrams for PS Joint

Using these values, a failure analysis was conducted with the Von Mises criteria since Aluminum is a ductile material. The Von Mises stress was calculated using the equation below for an element on top of the shaft that experiences the highest bending stress and one on the neutral axis of the shaft which experiences the highest transverse shear stress.

$$\sigma' = \sigma_{bending} \quad (3)$$

$$\sigma' = \sqrt{3}\tau_{transverse} \quad (4)$$

Using these hand calculations as a comparison, FEA was conducted using SolidWorks FEA to obtain a more accurate representation of the stresses given the complex geometry of the part. The part was modeled to have two bearing supports, which allowed for the ability to axially and rotationally constrain the part as well. This accounts for the retaining clip on the end of the shaft and the holding torque of the motor, allowing for the part to be exactly constrained. The vertical force was modeled to be applied to the threaded holes that connect the shaft to the differential mount. The moment load

was modeled to be applied on the face that mounts to the differential mount.

Because the PS joint has geometry consisting of several round edges from fillets, holes, and overall geometry, curvature-based mesh parameters were used to simulate loading on this part. The minimum element size was chosen to be 0.5 percent of the total length (0.27mm) to ensure that small features such as fillets and the feature

for the retaining ring were adequately represented. The maximum element size was chosen to be 5 percent of the total length (3 mm) to quickly geometry without generating unnecessary elements. For the minimum number of elements in a circle, 8 was chosen as a standard recommended value by SolidWorks for good balance.

Results

Firstly, from the free body diagram in Figure 15, the bearing support reactions at B1 and B2 were determined and compared with the rated radial loads supplied by McMaster-Carr [28] [29]. Bearing 1 experiences a reaction load of 655.1 N, with the rated maximum load of this bearing being 934 N (FOS of 1.4). Bearing 2 experiences a load of 715 N, with its rated maximum load being 4450 N (FOS of 6.2).

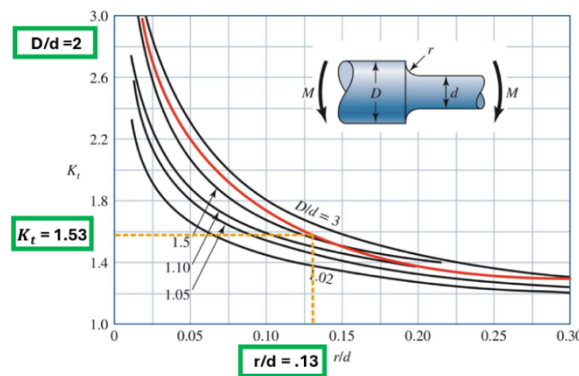


Figure 17: Stress Concentration Chart for Circular Beam in Bending [27]

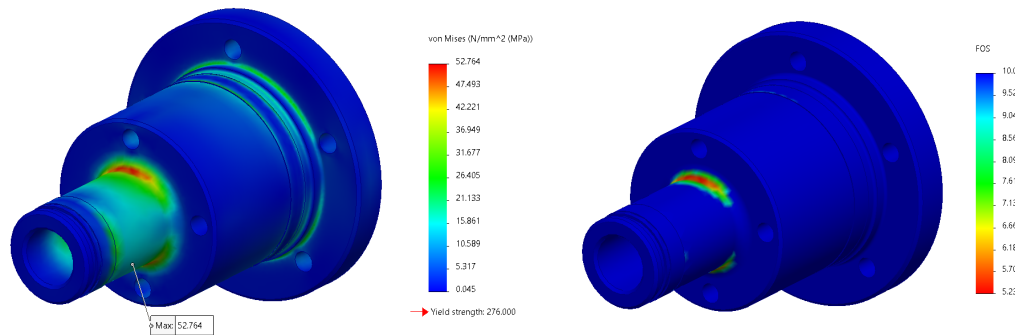


Figure 18: Von Mises Stresses (left) and Factor of Safety (right) for static loading condition

Additionally, from hand calculations, the highest stress was indicated to be on the smallest diameter shaft, with the maximum stress from bending being much higher than the transverse shear stress. The Von Mises stress of an element at the top of the smallest diameter shaft segment was calculated to be $\sigma' = 57.8 \text{ MPa}$. FEA produced equivalent results to hand calculations, with the highest stress concentration being exactly at the top of the fillet radius of the smallest shaft. The Von Mises stress here maxed at $\sigma' = 52.764 \text{ MPa}$. Aluminum 6061-T6 has a yield strength of 276 MPa, giving the shaft a FOS of 5.23.